

Direct Observation of Bandgap Oscillations Induced by Optical Phonons in Hybrid Lead Iodide Perovskites

Peijun Guo, Yi Xia, Jue Gong, Duyen H. Cao, Xiaotong Li, Xun Li, Qi Zhang, Constantinos C. Stoumpos, Matthew S. Kirschner, Haidan Wen, Vitali B. Prakapenka, John B. Ketterson, Alex B. F. Martinson, Tao Xu, Mercouri G. Kanatzidis, Maria K. Y. Chan, and Richard D. Schaller*

Hybrid organic–inorganic perovskites such as methylammonium lead iodide have emerged as promising semiconductors for energy-relevant applications. The interactions between charge carriers and lattice vibrations, giving rise to polarons, have been invoked to explain some of their extraordinary optoelectronic properties. Here, time-resolved optical spectroscopy is performed, with off-resonant pumping and electronic probing, to examine several representative lead iodide perovskites. The temporal oscillations of electronic bandgaps induced by coherent lattice vibrations are reported, which is attributed to antiphase octahedral rotations that dominate in the examined 3D and 2D hybrid perovskites. The off-resonant pumping scheme permits a simplified observation of changes in the bandgap owing to the A_g vibrational mode, which is qualitatively different from vibrational modes of other symmetries and without increased complexity of photogenerated electronic charges. The work demonstrates a strong correlation between the lead–iodide octahedral framework and electronic transitions, and provides further insights into the manipulation of coherent optical phonons and related properties in hybrid perovskites on ultrafast timescales.

1. Introduction

Hybrid organic–inorganic perovskites (HOIPs) as represented by methylammonium lead iodide (MAPbI₃) have garnered widespread interest owing to their promising applications in solar cells,^[1,2] solid-state lighting,^[3,4] detection of high-energy photons,^[5] in addition to exceptional physical responses and functions.^[6,7] Fundamental studies of their exceptionally long carrier lifetimes, good defect tolerance, and moderate mobility via various techniques have now indicated a polaronic character to charge carriers in HOIPs, which arises from the strong coupling of excited charge carriers with the dynamically disordered, soft inorganic lead–halide framework.^[8–15] Such polaronic properties may suppress unfavorable charge recombination and carrier trapping, thereby improving HOIP-based optoelectronic


Prof. P. Guo, Dr. Y. Xia, Dr. M. K. Y. Chan, Prof. R. D. Schaller
Center for Nanoscale Materials
Argonne National Laboratory
9700 South Cass Avenue, Lemont, IL 60439, USA
E-mail: schaller@anl.gov

Prof. P. Guo
Department of Chemical and Environmental Engineering
Yale University
9 Hillhouse Avenue, New Haven, CT 06520, USA

Dr. Y. Xia
Department of Materials Science and Engineering
Northwestern University
2220 Campus Drive, Evanston, IL 60208, USA

Dr. J. Gong, X. Li, Prof. T. Xu
Department of Chemistry and Biochemistry
Northern Illinois University
1425 W. Lincoln Hwy., DeKalb, IL 60115, USA

Dr. J. Gong
Department of Physics
Florida State University
77 Chieftan Way, Tallahassee, FL 32306, USA

 The ORCID identification number(s) for the author(s) of this article can be found under <https://doi.org/10.1002/adfm.201907982>.

DOI: 10.1002/adfm.201907982

Dr. D. H. Cao, Dr. A. B. F. Martinson
Materials Science Division
Argonne National Laboratory
9700 South Cass Avenue, Lemont, IL 60439, USA

X. Li, Prof. C. C. Stoumpos, Dr. M. S. Kirschner, Prof. M. G. Kanatzidis, Prof. R. D. Schaller
Department of Chemistry
Northwestern University
2145 Sheridan Road, Evanston, IL 60208, USA

Prof. Q. Zhang, Dr. H. Wen
Advanced Photon Source
Argonne National Laboratory
9700 South Cass Avenue, Lemont, IL 60439, USA

Prof. C. C. Stoumpos
Department of Materials Science and Technology
University of Crete
Vassilika Voutes, Heraklion GR-70013, Greece

Prof. V. B. Prakapenka
Center for Advanced Radiation Sources
University of Chicago
Chicago, IL 60637, USA

Prof. J. B. Ketterson
Department of Physics and Astronomy
Northwestern University
2145 Sheridan Road, Evanston, IL 60208, USA

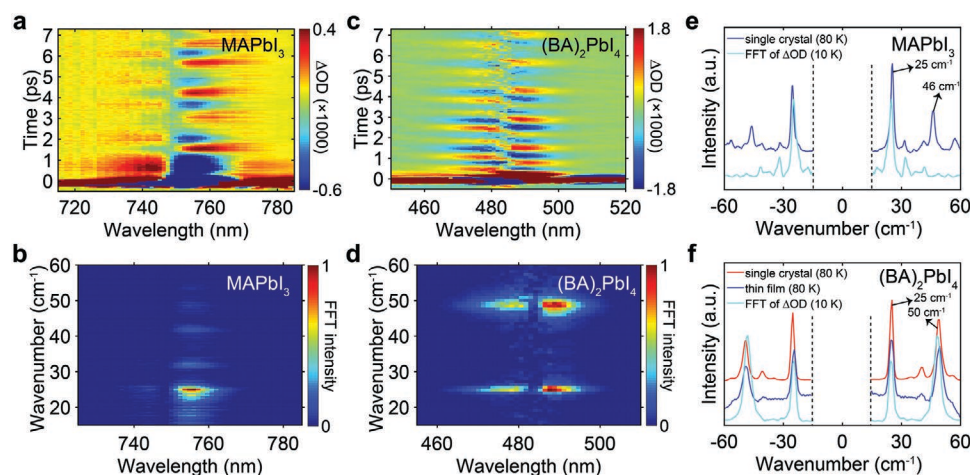


Figure 1. TA spectral maps and Raman spectra of MAPbI₃ and (BA)₂PbI₄. a) Transient ΔOD spectral map of the MAPbI₃ thin film measured at 10 K. b) FFT of the ΔOD map in (a). c) Transient ΔOD spectral map of the (BA)₂PbI₄ thin film measured at 10 K. d) FFT of the ΔOD map in (c). e) Raman spectrum of MAPbI₃ single crystal measured for the (010) surface at 80 K (blue), and FFT of the ΔOD kinetics extracted at 754 nm (cyan). f) Raman spectra of a (BA)₂PbI₄ single crystal (80 K, red), thin film (80 K, blue) and FFT of the ΔOD kinetics extracted at 490 nm (cyan). The pump in TA experiments was centered at 4 μm with a fluence of 1.4 mJ cm⁻². Data in (e) and (f) are offset for clarity.

devices. In this context, knowledge about how lattice vibrations, which dominate in HOIPs, impact their most critical optoelectronic properties, especially the electronic bandgap, is necessary to further understand the roles of electron–phonon interactions and polarons in HOIPs. Direct examination of such correlations, however, has proved challenging experimentally.

The structural similarity between 3D and 2D HOIPs, and materials composed of oxide octahedral networks (i.e., oxide perovskites), suggests that the experimental schemes developed for probing the photophysics and mutual interactions among different degrees of freedom in oxide perovskites might be generalized to the study of 3D and 2D HOIPs. In particular, excitation of infrared-active or Raman-active vibrational modes^[16] in oxide perovskites has been exploited to probe and control the magnetic order,^[17] electronic relaxation,^[18] and transient structural switching.^[19] Here we employ off-resonance excitation (without exciting charge carriers) with infrared pump pulses, to produce purely vibrationally excited lead–iodide perovskites through the impulsive stimulated Raman scattering mechanism. We then transiently probe the impacts of these coherent lattice vibrations on the valence-to-conduction-band electronic transitions and find that MAPbI₃ and several 2D lead–iodide perovskites exhibit a common Raman-active vibrational mode near 25 cm⁻¹. On the basis of first-principles calculations and symmetry analysis, we establish a microscopic picture of this pronounced vibrational mode. We further distinguish Raman-active, A_g vibrational modes from other Raman-active modes as well as from Raman-inactive modes and discuss the manifestation of these different types of modes in transient optical measurements.

2. Results and Discussion

The structural and morphological information for the MAPbI₃ and [CH₃(CH₂)₃NH₃]₂PbI₄ thin film samples used in this work is presented in Figure S1 of the Supporting Information. The

static absorption of an MAPbI₃ thin film on sapphire substrate (Figure S2a, Supporting Information) was examined as a function of temperature to establish a baseline for subsequent transient optical measurements. Since the exciton binding energy of MAPbI₃ remains nearly constant for the low-temperature (0–160 K) orthorhombic phase,^[20,21] the shift to lower energy of the exciton absorption peak with decreasing temperature mainly arises from a reduction of the bandgap (E_g); a concurrent narrowing of the exciton peak originates from reduced electron–phonon interactions.^[9] In transient absorption measurements, we perturb the MAPbI₃ film in the orthorhombic phase by nonresonant (i.e., nonabsorbing), sub-100 fs optical pump pulses centered at 4 μm , which is a scheme that is distinct from on-resonant electronic^[22] or vibrational^[23] excitations exploited elsewhere. A schematic experimental setup is shown in Figure S3 of the Supporting Information. The transient changes in optical density (denoted as ΔOD) comparing pump-on and pump-off conditions in the near-infrared wavelength range (Figure 1a) consist of a derivative-like line-shape, centered around the exciton peak at 750 nm, which oscillates above and below zero in sub-picosecond timescales. Such periodic oscillations, which signify coherent optical phonons (COPs), have been observed in (semi)metals,^[24] insulators,^[25,26] and semiconductors, including MAPbI₃ itself^[27,28] (but in the condition of above-bandgap optical pumping). A key feature of using non-resonant optical pumping here is that our data are completely free from parasitic electronic excitations; the latter usually give rise to large background in transient signals around the exciton peak due to a nonequilibrium redistribution of charge carriers near the band edge. Notably, from our data (Figure 1a) we find that E_g oscillates both above and below the static unperturbed value, an important point to be discussed in detail later. Note that the ΔOD amplitude on the red side of the exciton peak is consistently stronger in magnitude than that on the blue side of the exciton peak (Figure 1a), which stems from a lower slope of the static OD versus wavelength on the blue side of the exciton peak (Figure S2a, Supporting Information) due to contributions

to optical absorption from band-to-band transitions.^[21] A fast Fourier transform (FFT) plotted in Figure 1b demonstrates that the dominant COP of MAPbI₃ is centered at 25 cm⁻¹ (corresponding to 1.33 ps, or 0.75 THz), in conjunction with some higher-frequency modes with significantly weaker amplitudes.

To see if the nonresonant optical excitation of COPs is a general feature of HOIPs, we also examined (BA)₂PbI₄ (here BA stands for CH₃(CH₂)₃NH₃⁺),^[29] which is a member of the 2D HOIP family. 2D perovskites exhibit strong quantum and dielectric confinements of charge carriers and result in large exciton binding energies.^[30,31] Again, we observe strong signatures of COPs (Figure 1c) from a (BA)₂PbI₄ thin film excited at 4 μm, away from any resonances.^[32] The overall higher ΔOD amplitude of (BA)₂PbI₄ compared to that of MAPbI₃ is attributed to the sharper excitonic feature of the former (Figure S2b, Supporting Information). The FFT spectral map for (BA)₂PbI₄ (Figure 1d) displays two strong COP modes, centered at 25 and 50 cm⁻¹. To correlate available Raman modes with transient COPs, we performed low-frequency Raman scattering experiments on MAPbI₃ (Figure 1e) and (BA)₂PbI₄ (Figure 1f), using 946 and 659 nm lasers, respectively. These laser photon energies are below the *E_g* of the respective material and thereby do not introduce undesirable photoluminescence background. Note that with the 946 nm laser we could only obtain discernable Raman peaks from single crystals but not from thin films of MAPbI₃, which we interpret as resulting from a weak nonresonant Raman scattering cross section. An excellent match of the 25 cm⁻¹ phonon mode is observed between the Raman spectrum and the FFT of the transient COPs for MAPbI₃. Some of the higher-frequency modes in the Raman spectrum, especially that observed at 46 cm⁻¹, are not seen in the FFT of the transient response. This discrepancy may arise from the fact that the coupling strength of excitons with distinct vibrational modes can differ.^[33] The manifested 2:1 ratio in intensity of the 25 cm⁻¹ and the 46 cm⁻¹ peaks from single crystal measurements in Figure 1e do not translate to a 2:1 ratio in Raman scattering intensity of the respective phonon modes, because in a single crystal the thicknesses of MAPbI₃ contributing to the intensities of these two Raman peaks can differ; this makes a quantitative comparison between the Raman spectrum measured on single crystal, and FFT of the transient optical response measured from thin film, challenging. The agreement between the Raman scattering and transient optical measurements for (BA)₂PbI₄ in both the thin film and single crystal forms are exceptional over the entire frequency range up to 60 cm⁻¹. Although the higher-frequency (50 cm⁻¹) peak has almost twice the frequency of the lower-frequency one (25 cm⁻¹) for (BA)₂PbI₄, we rule out the possibility of overtone generation because the transient response (both Figure 1c,d) does include oscillation of *E_g* at 50 cm⁻¹.

In the following, we primarily focus on MAPbI₃ because the temperature dependence of *E_g* is clearer than that for (BA)₂PbI₄ (Figure S2, Supporting Information) and its vibrational properties can be more reliably calculated owing to the fully resolved orthorhombic crystal structure.^[34] First, fluence-dependent transient measurements were performed to determine the mechanism behind the excitation of COPs. As shown in Figure 2a,b, the amplitude of the transient response is linearly proportional to the pump fluence (rather than linear proportional to the electric field strength), suggesting an impulsive stimulated Raman

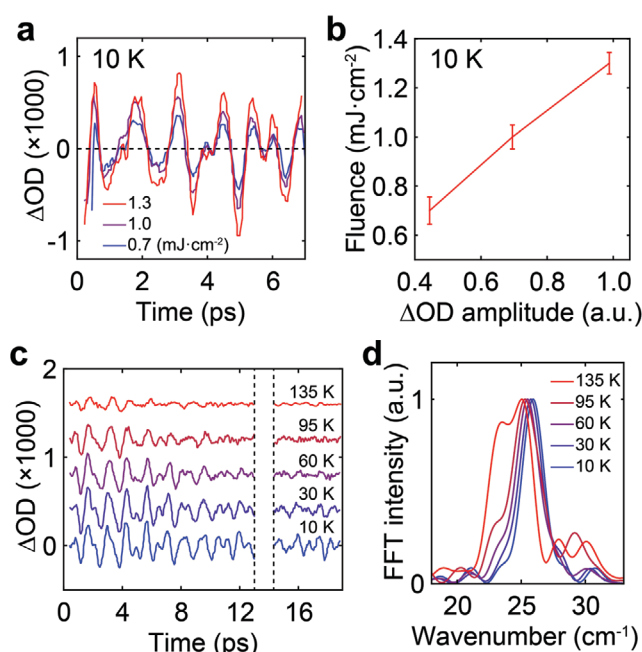


Figure 2. Temperature and fluence dependence of the transient optical response. a) Pump fluence dependent ΔOD kinetics of the MAPbI₃ film at 10 K. b) Extracted dependence of the ΔOD amplitude on the pump fluence from (a); error bars are generated by multiple measurements of the infrared pump power. c) Temperature-dependent ΔOD kinetics of the MAPbI₃ film at a fixed fluence of 0.53 mJ cm⁻². The region confined by the black-dashed lines contains coherent artifact due to pump reflection from the back of the substrates and are left out. d) FFT of the ΔOD kinetics shown in (c).

scattering (ISRS) process of excitation.^[35,36] In our earlier experiments, we found that pumping at other than 4 μm (e.g., at 3.2 μm) can also excite the same COPs.^[37] In ISRS, the non-resonant excitation pulse duration (less than 100 fs) is significantly shorter than a single period of the vibrational oscillation (about 1.3 ps here) and the phonon mode is Raman active (as verified by our Raman scattering measurements). Figure 2c,d presents the ΔOD kinetics and the corresponding FFT spectra measured at different temperatures. The coherence time is seen to decrease with increasing temperature, which we ascribe to more pronounced electron–phonon interactions at higher temperature. A small blueshift of the COP frequency is found to accompany the decrease of temperature due to stiffening of the lattice.^[38]

To resolve the microscopic atomic motions corresponding to the observed COP in MAPbI₃ at 25 cm⁻¹, we performed first-principles calculations of the vibrational normal modes for the orthorhombic phase of MAPbI₃, which belongs to the *Pnma* space group and has 48 atoms in a primitive cell.^[39,40] The definition of the crystalline *a*, *b*, and *c* axes are consistent with an earlier report,^[40] with the *b* axis being the long axis of the cell. Because the electronic density of states near the band edges are dominated by Pb and I atoms, here we confine our analysis to the first 72 phonon branches, since the 73rd to 144th branches have higher frequencies and are mainly contributed by motions of the MA cations^[40] and are hence irrelevant to our study (note that the frequency of the 73rd branch has an

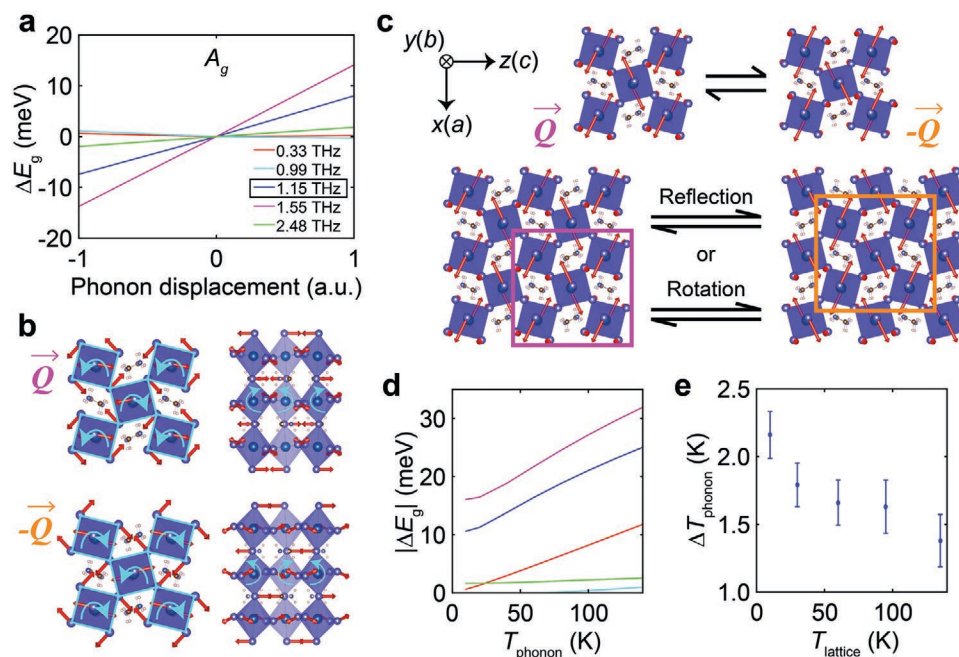


Figure 3. First-principles calculation of the vibrational modes and the associated ΔE_g . a) Correlation between the ΔE_g and the phonon displacements along the eigenvectors of the first five lowest-frequency A_g vibrational normal modes. b) Eigenvector of the A_g mode at 1.15 THz. Here \bar{Q} and $-\bar{Q}$ indicate the positive and negative phonon displacements, respectively. The orientation of the a, b and c axes are shown in c). c) Eigenvectors of the B_{2g} mode at 1.16 THz (top) and the schematics showing how the \bar{Q} and $-\bar{Q}$ configurations are related by different symmetry operations. d) Dependence of ΔE_g on the temperature for the A_g modes; legend of a) applies to d) as well. e) Estimated temperature rise of the 1.15 THz phonon following the ISRS process (the estimation is based on data shown in Figure 2c); error bars are generated from averaging the oscillation amplitude of the first three oscillations.

abrupt jump to 9.94 THz from 4.56 THz for the 72nd branch). Table S1 in the Supporting Information summarizes the band indices, frequencies and irreducible representations of the 72 normal modes. The schematic drawing of a typical mode profile for each representation (including A_g , B_{1g} , B_{2g} , B_{3g} , A_u , B_{1u} , B_{2u} , and B_{3u}) is shown in Figure S4 of the Supporting Information. To correlate the calculated normal modes with the E_g oscillations arising from the COP, we computed the change of E_g (designated as ΔE_g) due to phonon displacements for all 72 phonon branches. **Figure 3a** shows the calculated ΔE_g due to phonon displacements along both the positive and negative directions for the 5 lowest-frequency A_g modes (out of the eight A_g modes in total; see Table S1, Supporting Information). Note that all the plots of ΔE_g versus phonon displacement in Figure 3a exhibit asymmetric line-shapes around the equilibrium configuration (i.e., at zero phonon displacement). In contrast, for all the non- A_g modes (such as B_{1g} , B_{2g} , etc), the ΔE_g is symmetric with respect to positive and negative displacements (Figure S5, Supporting Information). Because the E_g oscillates both above and below the static value in the transient measurements, we must assign the ISRS-driven COP to one of the A_g modes (which are all Raman active). Here, we assign the COP to the 1.15 THz mode, which is schematically illustrated in Figure 3b. As plotted in Figure 3a, the 1.15 THz mode induces large and nearly linear ΔE_g in both the positive and negative directions in distinction from the other vibrational modes (i.e., the ones at 0.33, 0.99, and 2.48 THz). We do not eliminate the possibility that the 0.99 THz or the 1.55 THz mode is responsible for the observed COP. Nevertheless, each of the three modes (the 1.15-, 0.99-, and 1.55 THz modes as depicted in

Figure 3b, Figure S6b,c in the Supporting Information) involves mainly the antiphase octahedral rotation within the a - c plane as well as the a - b plane (the three axes are defined in Figure 3c), although of different weights: for example, the 1.15 THz mode has a stronger contribution through octahedral rotations in the a - c plane, whereas rotations for the 0.99- and 1.55-THz modes are more distributed in the a - b plane. Here, antiphase means that two corner-connected octahedra rotate along opposite directions (i.e., one clockwise and the other counterclockwise).

As illustrated in Figure 3c for a Raman-active B_{2g} mode at 1.16 THz (as an example), any vibrational normal mode with irreducible representation other than A_g possesses some characters of “-1” (see ref. [41]); the corresponding symmetry operations (examples in Figure 3c include a mirror reflection in the a - b plane or a 180° rotation along the c axis) force the positively displaced as well as the negatively displaced configurations to be degenerate, leading to the symmetric ΔE_g with respect to phonon displacements (Figure S5, Supporting Information). This type of degeneracy should lead to an observed oscillation frequency in transient optical experiments that is twice that of the frequency of the corresponding vibrational normal mode. Such degeneracy also results in the zero first-order derivative of ΔE_g with phonon displacement near the origin (Figure S5, Supporting Information), hence dictating a negligible ΔE_g under very small perturbations, and the ΔE_g should also scale quadratically with the pump power. This is in sharp contrast to the dependence of ΔE_g on phonon displacement for the A_g modes, which exhibits a finite first-order derivative near the equilibrium (Figure 3a). For the same reason, the change of other material properties (such as efficiency of

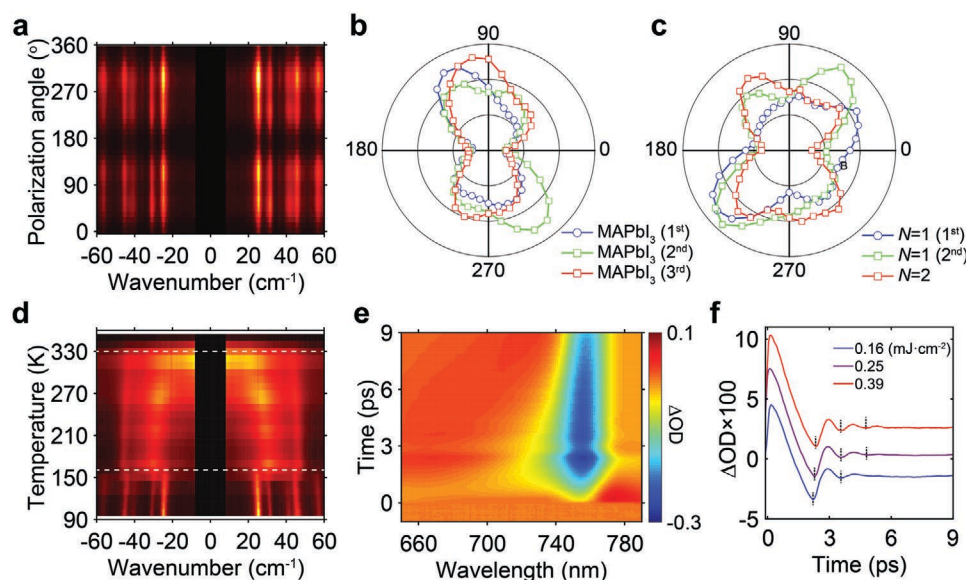


Figure 4. Low-frequency Raman spectra and transient optical response from above-bandgap optical pumping. a) Polarization-angle dependence of the Raman spectrum for a MAPbI₃ single crystal measured on the (010) surface at 80 K; 0° is defined to be parallel to the [100] direction defined in the tetragonal phase. Correlation of the intensity of the 25 cm⁻¹ Raman peak with the polarization angle for MAPbI₃ in b), and for $N = 1$ and $N = 2$ in c). d) Raman spectra of MAPbI₃ as a function of temperature measured on the (010) surface (crystalline direction here is defined in the orthorhombic phase); the literature reported temperatures of phase transitions^[64] (161 and 330 K) are indicated by the white-dashed lines. e) Transient ΔOD spectral map acquired using 400 nm pump measured at 10 K under a fluence of 0.16 mJ cm⁻². f) Dependence of ΔOD kinetics (taken at 782 nm) for MAPbI₃ on the pump fluence. Curves in f) are offset for clarity.

second harmonic generation, polarizability, spontaneous polarization, elasticity, etc) arising from the displacements along a non- A_g vibrational normal mode is expected to vanish at very small displacement amplitude. This argument may, in part, explain the dominant appearance of A_g modes in ultrafast ISRS investigations as reported elsewhere,^[35,42,43] even though the ISRS process does not preclude the excitation of other non- A_g , Raman-active vibrational modes (such as B_{1g} , B_{2g} , and B_{3g} modes in the present case).

In experiments where free electrons were directly excited by the pump pulse,^[44] the two-temperature model has been frequently invoked to determine the strength of electron–phonon interactions. In the present case, the particular A_g vibrational mode at 25 cm⁻¹ was excited and then relaxes through various dissipation channels by phonon–phonon and phonon–electron interactions. With experimental and computational data in hand, we are positioned to estimate the effective temperature rise for the 25 cm⁻¹ phonon mode following ISRS before any dissipation processes of the COP take place. We first identify the dependence of the static OD on the lattice temperature measured using the white light probe in the transient absorption setup with the pump beam blocked (Figure S7, Supporting Information), which permits us to evaluate the magnitude of ΔE_g in accordance with the amplitude of ΔOD , for which we average over the first 3 periods of oscillation (Figure 2c) at different lattice temperatures. The ΔE_g are determined to be in the range of 0.3 to 0.1 meV, which varies with lattice temperature from 10 to 135 K. Based on the first-principles calculated ΔE_g induced by the change of the temperature (T_{ph}) of the A_g phonon modes (with temperatures of all the other phonon branches fixed) shown in Figure 3d, we can then assess the rise of phonon temperature

of the A_g phonon modes measured at different lattice temperatures. The result is shown in Figure 3e if we assume the excited COP correspond to the 1.15 THz phonon mode. We find that the temperature rise of the 1.15 THz mode is in the range of 1 to 2 K (under the same fluence) and decreases with increasing lattice temperature. Note that different ΔT_{ph} plots can result if we associate the COP to the 0.99 or 1.55 THz mode.

As the transient optical measurements were based on polycrystalline thin film samples, for which the crystal-direction-dependent properties are lost, we further performed polarization-dependent Raman scattering measurements on single crystalline MAPbI₃ for the (010) surface of the orthorhombic phase. Note that the [001] direction defined for the tetragonal phase of MAPbI₃ is along the long axis; this long axis is changed to the b -axis, or the [010] direction for the orthorhombic phase.^[40] As shown in Figure 4a, the shape of the Raman scattering spectrum is maintained for different polarization angles, but the intensities of the peaks vary with the polarization angle in a uniform fashion and exhibit a quasi-fourfold symmetric pattern as demonstrated in Figure 4b. An exact fourfold symmetric intensity distribution is not expected because the measurements were performed for the orthorhombic but not for the tetragonal phase, where the former phase does not have fourfold rotational symmetry along the long axis. On-average, the Raman scattering efficiency is found to peak at 45° from the main crystalline axis. However, we found that the angular distribution of the peak intensity can slightly vary from spot to spot and from crystal to crystal, since the sudden changes in the lattice parameters on going from the tetragonal to the orthorhombic phase may result in the formation of polycrystalline domains^[45] or incommensurately

modulated structures^[46] in HOIPs. Interestingly, additional Raman scattering measurements along the long axis, cross-plane direction of $(\text{BA})_2\text{PbI}_4$ and $(\text{BA})_2(\text{MA})\text{Pb}_2\text{I}_7$ (denoted as $N = 1$ and $N = 2$ in the plots) reveal similar fourfold patterns in the polar plot of the Raman intensity with polarization angle (Figure 4c and Figure S8 in the Supporting Information), and all three materials (MAPbI_3 , $N = 1$ and $N = 2$) exhibit a strong Raman peak at 25 cm^{-1} , which may arise from very similar, if not identical, inorganic-framework dominated antiphase octahedral rotations. In fact, transient optical measurements on additional Pb–I based 2D HOIPs all reveal the prevailing transient response at 25 cm^{-1} (Figure S9, Supporting Information), which are not infrared-active (Figure S10 in the Supporting Information). Note that we did not observe any transient oscillations from the tetragonal phase of MAPbI_3 , which is consistent with the temperature dependent Raman spectra (Figure 4d) that exhibit diffuse Raman central peaks in the cubic and tetragonal phases, resembling the Raman scattering characteristics of MAPbBr_3 and CsPbBr_3 , as reported elsewhere.^[10]

Finally, we compare the $4\text{ }\mu\text{m}$ excitation results with those obtained from above-bandgap pumping experiments. Figure 4e displays a transient spectral map acquired using 400 nm pumping, and selected kinetics are plotted in Figure 4f for different pump fluences. Although the signatures of COPs are still discernable, they appear to decohere much more rapidly in comparison to those shown in Figure 1a. Furthermore, the initial oscillation amplitude of ΔOD is more than one order of magnitude stronger than that achieved using $4\text{ }\mu\text{m}$ pumping. We attribute these observations to strong interactions of charge carriers with the COPs, which can impulsively drive the COP through electron–phonon interactions during the sub-pico-second hot carrier relaxation process (which is more efficient than the ISRS process) but can also scatter and cause the COP to lose coherence more rapidly.

3. Conclusion

We have employed off-resonance infrared optical pumping to examine the dominant lattice vibration response of MAPbI_3 in an extremely clean fashion and delineated the associated impact on the electronic bandgap of the material, which is corroborated by symmetry arguments and first-principles calculations. Our observations are consistent with the formation of a rotationally disordered octahedral network in the tetragonal phase of MAPbI_3 as determined from MeV ultrafast electron diffraction experimentation,^[11] as well as the spontaneous symmetry breaking in the respective cubic phase.^[47] Our work sheds light on further manipulating COPs in the structurally diverse HOIPs^[48] for the generation of effective magnetic fields^[17] as well as the access to nonequilibrium ferroelectric phases^[6,25,26] and quantum phases,^[49,50] which have been previously pursued with materials such as oxide perovskites. The similarity (and difference) of the rotations of octahedra between 3D and 2D hybrid perovskites, and between inorganic and hybrid perovskites, are among the remaining questions, since it has been demonstrated that hydrogen bonding plays an important role in mediating the octahedral tilts.^[51] Another intriguing question for MAPbI_3 is whether the lattice vibration following

the ultrafast laser excitation initiates toward positive or negative phonon displacements, and its correlation with the initial change of the bandgap, which can be further investigated with ultrafast electron^[52] or X-ray diffraction methods. Such investigation may provide hints for the anomalous dependence of the bandgap of MAPbI_3 on lattice temperature.

4. Experimental Section

Fabrication of MAPbI_3 Sample: Methylamine solution (CH_3NH_2 , 40 wt% in H_2O) and N-methyl-2-pyrrolidinone (NMP) were purchased from Aldrich. Hydriodic acid (HI, 57 wt% in H_2O) and lead iodide (PbI_2 , 99.9985% metals basis) were purchased from Alfa Aesar. Ethyl ether (anhydrous) and acetone were obtained from Fisher Chemical. All chemicals were used as received without further purification. $\text{CH}_3\text{NH}_3\text{I}$ was synthesized by dropwise adding equimolar of HI to react with CH_3NH_2 with stirring in a 100 mL round bottom flask, which was soaked in ice bath to slow heat generation. Next, the mixture solution was rotary evaporated at $60\text{ }^\circ\text{C}$ to dry off the water. Then, as-formed yellow solid was washed with copious amount of ethyl ether on a filter paper and followed by vacuum filtration. The $\text{CH}_3\text{NH}_3\text{I}$ powder thereby obtained was dried in a vacuum oven at $60\text{ }^\circ\text{C}$ overnight to yield pure product. Fabrication of MAPbI_3 thin film follows the method reported previously^[53] with slight modifications. In detail, 1:1 molar ratio of $\text{CH}_3\text{NH}_3\text{I}$ and PbI_2 was dissolved in NMP to make 40 wt% precursor solution. The precursor solution was spin-coated on acetone-cleaned sapphire substrate at 3000 rpm for 25 s. The wet film was then quickly immersed in a 50 mL ethyl ether bath for 2 min, after which the as-formed $\text{CH}_3\text{NH}_3\text{PbI}_3$ thin film was annealed at $100\text{ }^\circ\text{C}$ for 10 min in a humidity-controlled atmosphere with a petri dish covered atop.

Fabrication of 2D Perovskite Samples: Single crystals of $(\text{BA})_2\text{PbI}_4$ and $(\text{BA})_2(\text{MA})\text{Pb}_2\text{I}_7$ crystals were synthesized according to previously published method.^[29] $(\text{BA})_2\text{PbI}_4$ perovskite precursor solution was prepared by dissolving presynthesized $(\text{BA})_2\text{PbI}_4$ crystals (0.432 g, 0.5 mmol) in 1 mL DMF to make a 0.5 M solution. $(\text{BA})_2(\text{MA})\text{Pb}_2\text{I}_7$ perovskite precursor solution was prepared by dissolving presynthesized $(\text{BA})_2(\text{MA})\text{Pb}_2\text{I}_7$ crystals (1.483 g, 0.2 mmol) in 1 mL DMF to make a 0.1 M solution. The solution was stirred on a $75\text{ }^\circ\text{C}$ hot plate for 1 h, subsequently filtered using a $0.45\text{ }\mu\text{m}$ filter, and kept on the $75\text{ }^\circ\text{C}$ hot plate throughout the thin film fabrication process. The $(\text{BA})_2\text{PbI}_4$ and $(\text{BA})_2(\text{MA})\text{Pb}_2\text{I}_7$ films were fabricated by spin-coating $75\text{ }\mu\text{L}$ of the perovskite solution on sapphire substrates at 7000 rpm (1200 rpm for samples used for THz measurements) for 30 s. After the spin-coating process ended, the samples were immediately transferred to a $100\text{ }^\circ\text{C}$ hot plate for annealing for 5 min. The substrates were cleaned via ultrasonication in acetone, isopropanol, and further subjected to ozone cleaning (Jelight Company, Inc., Model 18) for 10 min before use. The precursor solution preparation and the thin film fabrication were done in a N_2 glovebox.

Optical Characterization: A custom setup was employed for static optical absorption experiments. Transient absorption measurements were performed using a 35 fs amplified Ti:sapphire laser operating at 800 nm at a repetition rate of 2 kHz. The broadband probe pulses were generated by focusing a portion of the amplifier output onto an Al_2O_3 window. The MIR pump pulses were generated via difference frequency mixing of signal and idler beams with an optical parametric amplifier and were reduced in repetition rate down to 1 kHz. The 400 nm pump pulses were produced by frequency doubling of the 800 nm amplifier output with a BBO crystal. The probe pulses were mechanically time-delayed using a translation stage and retroreflector. Low frequency Raman spectra were acquired using 946 nm laser excitation for MAPbI_3 and 659 nm for layered perovskites ($N = 1$ and $N = 2$). A description of the Raman system has been published elsewhere.^[54] The samples were mounted in a cold-finger liquid-nitrogen or closed-cycle helium cryostat under a pressure below 1×10^{-7} Torr. Two notch filters were used to suppress the Rayleigh scattering, so that Raman signals with frequencies down to 10 cm^{-1} can

be captured. All the Raman spectra were acquired with a 20× objective under the parallel configuration. For the THz time-domain spectroscopy, a 1 mm thick (110) ZnTe crystal was excited by 35 fs, 800 nm pulses from a Ti:sapphire amplifier at 1 kHz repetition rate to generate THz pulses. Another identical ZnTe crystal was used to detect the transmitted THz pulses via the standard electro-optic sampling technique.

First-Principles Calculations of the Electronic Structure and Lattice Dynamics: First-principles calculations based on the density functional theory using the Vienna Ab initio Simulation Package (VASP) were performed.^[55–58] The generalized gradient approximation (GGA)^[59] for the exchange–correlation functional^[60] within the context of the projector augmented wave method^[61] as implemented in VASP was used. In order to treat the dispersion forces from nonlocal electron–electron interactions more properly, the van der Waals density functional (vdW-DF) method was adopted, particularly, the optB86b-vdW functional.^[62] The crystal structure of MAPbI₃ in this study adopts the orthorhombic phase with the *Pnma* space group (No. 62). The structure was fully relaxed using a $4 \times 4 \times 4$ Γ -centered *k*-point mesh with a kinetic energy cutoff of 550 eV. The convergence thresholds for the total energy and residual force are 10^{-8} eV and 5×10^{-3} eV Å⁻¹, respectively. Since the phonon modes relevant in the experiments are in the long wavelength limit, the phonon frequencies and eigenvectors at the Γ point using the unit cell by means of finite-displacement method as implemented in Phonopy were calculated,^[63] as well as a comprehensive group-theoretical analysis of the normal modes of vibrations. In order to reveal the correlation between the change in the bandgap and the phonon displacements relevant to a given vibrational normal mode, the bandgap was calculated as a function of atomic positions, which are displaced according to a given phonon mode, namely, $\pm A_s^\sigma \epsilon_s^\sigma$, where ϵ_s^σ is the normalized phonon mode eigenvector and A_s^σ is the vibrational amplitude, which is defined as $A_s^\sigma = \sqrt{\frac{\hbar}{M_\sigma \omega_s} \left[\frac{1}{2} + n \left(\frac{\hbar \omega_s}{k_B T} \right) \right]}$,

where *s* and σ index the phonon branch and the atom, respectively. *M*, ω , *n*, and *T* are the atomic mass, phonon frequency, phonon population and temperature, respectively. As a result of this equation, a correlation between the change in the bandgap and the temperature of a specific phonon mode can be established, as depicted in Figure 3d.

Supporting Information

Supporting Information is available from the Wiley Online Library or from the author.

Acknowledgements

This work was performed, in part, at the Center for Nanoscale Materials, a U.S. Department of Energy Office of Science User Facility, and supported by the U.S. Department of Energy, Office of Science, under Contract No. DE-AC02-06CH11357. Work at Northwestern was supported by grant SC0012541 from the U.S. Department of Energy, Office of Science (sample preparation and structural characterization). T.X. acknowledges the financial support from National Science Foundation (DMR-1806152). Raman measurements were performed at GeoSoilEnviroCARS (The University of Chicago, Sector 13), Advanced Photon Source (APS), Argonne National Laboratory. Work by A.B.F.M. and D.H.C. was supported by the Center for Light Energy Activated Redox Processes (LEAP), an Energy Frontier Research Center funded by the U.S. Department of Energy, Office of Science, Office of Basic Energy Sciences under Award DE-SC0001059. GeoSoilEnviroCARS was supported by the National Science Foundation – Earth Sciences (EAR – 1634415). The Raman system acquisition was supported by the NSF MRI proposal (EAR-1531583). Q.Z. and H.W. acknowledge the support by the U.S. Department of Energy, Office of Science, under Contract No. DE-SC0012509. The authors thank Nicholas Holtgrewe for help with the Raman measurements and Pierre Darancet for discussions.

Conflict of Interest

The authors declare no conflict of interest.

Author Contributions

P.G. and Y. X. contributed equally to this work. P.G. conceived and performed the measurements under the supervision of R.D.S. Y.X. performed first-principles calculations under the supervision of M.K.Y.C. P.G. and Y.X. conceptualized the symmetry argument of the observed vibrational mode. J.G., D.H.C., C.C.S., Xiaotong L., and Xun L. fabricated the samples under the supervision of T.X., A.B.F.M., and M.K.G. V.B.P., Q.Z., and H.W. assisted with Raman and THz experiments. J.B.K. contributed to the analysis of the results. P.G. wrote the manuscript with input from coauthors. R.D.S. supervised the project.

Keywords

coherent optical phonons, electron–phonon coupling, hybrid perovskites, Raman scattering, transient optical spectroscopy

Received: September 26, 2019

Revised: February 27, 2020

Published online:

- [1] M. M. Lee, J. Teuscher, T. Miyasaka, T. N. Murakami, H. J. Snaith, *Science* **2012**, 338, 643.
- [2] H. Zhou, Q. Chen, G. Li, S. Luo, T.-B. Song, H.-S. Duan, Z. Hong, J. You, Y. Liu, Y. Yang, *Science* **2014**, 345, 542.
- [3] H. Zhu, Y. Fu, F. Meng, X. Wu, Z. Gong, Q. Ding, M. V. Gustafsson, M. T. Trinh, S. Jin, X.-Y. Zhu, *Nat. Mater.* **2015**, 14, 636.
- [4] Y. Jia, R. A. Kerner, A. J. Grede, B. P. Rand, N. C. Giebink, *Nat. Photonics* **2017**, 11, 784.
- [5] S. Yakunin, M. Sytnyk, D. Kriegner, S. Shrestha, M. Richter, G. J. Matt, H. Azimi, C. J. Brabec, J. Stangl, M. V. Kovalenko, W. Heiss, *Nat. Photonics* **2015**, 9, 444.
- [6] Y.-M. You, W.-Q. Liao, D. Zhao, H.-Y. Ye, Y. Zhang, Q. Zhou, X. Niu, J. Wang, P.-F. Li, D.-W. Fu, Z. Wang, S. Gao, K. Yang, J.-M. Liu, J. Li, Y. Yan, R.-G. Xiong, *Science* **2017**, 357, 306.
- [7] B. Chen, T. Li, Q. Dong, E. Mosconi, J. Song, Z. Chen, Y. Deng, Y. Liu, S. Ducharme, A. Gruverman, F. De Angelis, J. Huang, *Nat. Mater.* **2018**, 17, 1020.
- [8] K. Miyata, D. Meggiolaro, M. T. Trinh, P. P. Joshi, E. Mosconi, S. C. Jones, F. De Angelis, X.-Y. Zhu, *Sci. Adv.* **2017**, 3, e1701217.
- [9] A. D. Wright, C. Verdi, R. L. Milot, G. E. Eperon, M. A. Pérez-Osorio, H. J. Snaith, F. Giustino, M. B. Johnston, L. M. Herz, *Nat. Commun.* **2016**, 7, 11755.
- [10] O. Yaffe, Y. Guo, L. Z. Tan, D. A. Egger, T. Hull, C. C. Stoumpos, F. Zheng, T. F. Heinz, L. Kronik, M. G. Kanatzidis, J. S. Owen, A. M. Rappe, M. A. Pimenta, L. E. Brus, *Phys. Rev. Lett.* **2017**, 118, 136001.
- [11] X. Wu, L. Z. Tan, X. Shen, T. Hu, K. Miyata, M. T. Trinh, R. Li, R. Coffee, S. Liu, D. A. Egger, I. Makasyuk, Q. Zheng, A. Fry, J. S. Robinson, M. D. Smith, B. Guzelturk, H. I. Karunadasa, X. Wang, X. Zhu, L. Kronik, A. M. Rappe, A. M. Lindenberg, *Sci. Adv.* **2017**, 3, e1602388.
- [12] K. T. Munson, E. R. Kennehan, J. B. Asbury, *J. Mater. Chem. C* **2019**, 7, 5889.
- [13] M. Park, N. Kornienko, S. E. Reyes-Lillo, M. Lai, J. B. Neaton, P. Yang, R. A. Mathies, *Nano Lett.* **2017**, 17, 4151.

- [14] M. Park, A. J. Neukirch, S. E. Reyes-Lillo, M. Lai, S. R. Ellis, D. Dietze, J. B. Neaton, P. Yang, S. Tretiak, R. A. Mathies, *Nat. Commun.* **2018**, 9, 2525.
- [15] X.-Y. Zhu, V. Podzorov, *J. Phys. Chem. Lett.* **2015**, 6, 4758.
- [16] M. Först, R. Mankowsky, A. Cavalleri, *Acc. Chem. Res.* **2015**, 48, 380.
- [17] T. F. Nova, A. Cartella, A. Cantaluppi, M. Först, D. Bossini, R. V. Mikhaylovskiy, A. V. Kimel, R. Merlin, A. Cavalleri, *Nat. Phys.* **2017**, 13, 132.
- [18] G. Coslovich, B. Huber, W.-S. Lee, Y.-D. Chuang, Y. Zhu, T. Sasagawa, Z. Hussain, H. A. Bechtel, M. C. Martin, Z. X. Shen, R. W. Schoenlein, R. A. Kaindl, *Nat. Commun.* **2013**, 4, 2643.
- [19] D. M. Juraschek, M. Fechner, N. A. Spaldin, *Phys. Rev. Lett.* **2017**, 118, 054101.
- [20] A. Miyata, A. Mitioglu, P. Plochocka, O. Portugall, J. T.-W. Wang, S. D. Stranks, H. J. Snaith, R. J. Nicholas, *Nat. Phys.* **2015**, 11, 582.
- [21] C. L. Davies, M. R. Filip, J. B. Patel, T. W. Crothers, C. Verdi, A. D. Wright, R. L. Milot, F. Giustino, M. B. Johnston, L. M. Herz, *Nat. Commun.* **2018**, 9, 293.
- [22] M. B. Price, J. Butkus, T. C. Jellicoe, A. Sadhanala, A. Briane, J. E. Halpert, K. Broch, J. M. Hodgkiss, R. H. Friend, F. Deschler, *Nat. Commun.* **2015**, 6, 8420.
- [23] M. Grechko, S. A. Bretschneider, L. Vietze, H. Kim, M. Bonn, *Angew. Chem., Int. Ed.* **2018**, 57, 13657.
- [24] M. Hase, K. Mizoguchi, H. Harima, S. Nakashima, M. Tani, K. Sakai, M. Hangyo, *Appl. Phys. Lett.* **1996**, 69, 2474.
- [25] X. Li, T. Qiu, J. Zhang, E. Baldini, J. Lu, A. M. Rappe, K. A. Nelson, *Science* **2019**, 364, 1079.
- [26] T. F. Nova, A. S. Disa, M. Fechner, A. Cavalleri, *Science* **2019**, 364, 1075.
- [27] H. Wang, L. Valkunas, T. Cao, L. Whittaker-Brooks, G. R. Fleming, *J. Phys. Chem. Lett.* **2016**, 7, 3284.
- [28] C. M. Mauck, A. France-Lanord, A. C. H. Oendra, N. S. Dahod, J. C. Grossman, W. A. Tisdale, *J. Phys. Chem. C* **2019**, 123, 27904.
- [29] C. C. Stoumpos, D. H. Cao, D. J. Clark, J. Young, J. M. Rondinelli, J. I. Jang, J. T. Hupp, M. G. Kanatzidis, *Chem. Mater.* **2016**, 28, 2852.
- [30] L. N. Quan, M. Yuan, R. Comin, O. Voznyy, E. M. Beauregard, S. Hoogland, A. Buin, A. R. Kirmani, K. Zhao, A. Amassian, D. H. Kim, E. H. Sargent, *J. Am. Chem. Soc.* **2016**, 138, 2649.
- [31] P. Guo, W. Huang, C. C. Stoumpos, L. Mao, J. Gong, L. Zeng, B. T. Diroll, Y. Xia, X. Ma, D. J. Gosztola, T. Xu, J. B. Ketterson, M. J. Bedzyk, A. Facchetti, T. J. Marks, M. G. Kanatzidis, R. D. Schaller, *Phys. Rev. Lett.* **2018**, 121, 127401.
- [32] P. Guo, J. Gong, S. Sadasivam, Y. Xia, T.-B. Song, B. T. Diroll, C. C. Stoumpos, J. B. Ketterson, M. G. Kanatzidis, M. K. Y. Chan, P. Darancet, T. Xu, R. D. Schaller, *Nat. Commun.* **2018**, 9, 2792.
- [33] F. Thouin, D. A. Valverde-Chávez, C. Quarti, D. Cortecchia, I. Bargigia, D. Beljonne, A. Petrozza, C. Silva, A. R. Srimath Kandada, *Nat. Mater.* **2019**, 18, 349.
- [34] T. Baikie, Y. Fang, J. M. Kadro, M. Schreyer, F. Wei, S. G. Mhaisalkar, M. Graetzel, T. J. White, *J. Mater. Chem. A* **2013**, 1, 5628.
- [35] L. Dhar, J. A. Rogers, K. A. Nelson, *Chem. Rev.* **1994**, 94, 157.
- [36] C. Fei, J. S. Sarmiento, H. Wang, *J. Phys. Chem. C* **2018**, 122, 17035.
- [37] P. Guo, A. Mannodi-Kanakkithodi, J. Gong, Y. Xia, C. C. Stoumpos, D. H. Cao, B. T. Diroll, J. B. Ketterson, G. P. Wiederrecht, T. Xu, M. K. Y. Chan, M. G. Kanatzidis, R. D. Schaller, *Nat. Commun.* **2019**, 10, 482.
- [38] P. Guo, Y. Xia, J. Gong, C. C. Stoumpos, K. M. McCall, G. C. B. Alexander, Z. Ma, H. Zhou, D. J. Gosztola, J. B. Ketterson, M. G. Kanatzidis, T. Xu, M. K. Y. Chan, R. D. Schaller, *ACS Energy Lett.* **2017**, 2, 2463.
- [39] F. Brivio, J. M. Frost, J. M. Skelton, A. J. Jackson, O. J. Weber, M. T. Weller, A. R. Goñi, A. M. A. Leguy, P. R. F. Barnes, A. Walsh, *Phys. Rev. B* **2015**, 92, 144308.
- [40] M. A. Pérez-Osorio, R. L. Milot, M. R. Filip, J. B. Patel, L. M. Herz, M. B. Johnston, F. Giustino, *J. Phys. Chem. C* **2015**, 119, 25703.
- [41] M. S. Dresselhaus, G. Dresselhaus, A. Jorio, *Group Theory - Application to the Physics of Condensed Matter*, Springer, Leipzig, Germany **2008**.
- [42] D. M. Fritz, D. A. Reis, B. Adams, R. A. Akre, J. Arthur, C. Blome, P. H. Bucksbaum, A. L. Cavalieri, S. Engemann, S. Fahy, R. W. Falcone, P. H. Fuoss, K. J. Gaffney, M. J. George, J. Hajdu, M. P. Hertlein, P. B. Hillyard, M. Horn-von Hoegen, M. Kammrler, J. Kaspar, R. Kienberger, P. Krejčík, S. H. Lee, A. M. Lindenberg, B. McFarland, D. Meyer, T. Montagne, É. D. Murray, A. J. Nelson, M. Nicoul, R. Pahl, J. Rudati, H. Schlarb, D. P. Siddons, K. Sokolowski-Tinten, Th. Tschentscher, D. von der Linde, J. B. Hastings, *Science* **2007**, 315, 633.
- [43] M. Porer, M. Fechner, E. M. Bothschafter, L. Rettig, M. Savoini, V. Esposito, J. Rittmann, M. Kubli, M. J. Neugebauer, E. Abreu, T. Kubacka, T. Huber, G. Lantz, S. Parchenko, S. Gröbel, A. Paarmann, J. Noack, P. Beaud, G. Ingold, U. Aschauer, S. L. Johnson, U. Staub, *Phys. Rev. Lett.* **2018**, 121, 055701.
- [44] P. Guo, R. D. Schaller, J. B. Ketterson, R. P. H. Chang, *Nat. Photonics* **2016**, 10, 267.
- [45] P. S. Whitfield, N. Herron, W. E. Guise, K. Page, Y. Q. Cheng, I. Milas, M. K. Crawford, *Sci. Rep.* **2016**, 6, 35685.
- [46] Y. Guo, O. Yaffe, D. W. Paley, A. N. Beecher, T. D. Hull, G. Szpak, J. S. Owen, L. E. Brus, M. A. Pimenta, *Phys. Rev. Mater.* **2017**, 1, 042401(R).
- [47] A. N. Beecher, O. E. Semonin, J. M. Skelton, J. M. Frost, M. W. Terban, H. Zhai, A. Alatas, J. S. Owen, A. Walsh, S. J. L. Billinge, *ACS Energy Lett.* **2016**, 1, 880.
- [48] W. Li, Z. Wang, F. Deschler, S. Gao, R. H. Friend, A. K. Cheetham, *Nat. Rev. Mater.* **2017**, 2, 16099.
- [49] D. N. Basov, R. D. Averitt, D. Hsieh, *Nat. Mater.* **2017**, 16, 1077.
- [50] M. Gu, J. M. Rondinelli, *Phys. Rev. B* **2018**, 98, 024102.
- [51] J.-H. Lee, N. C. Bristowe, J. H. Lee, S.-H. Lee, P. D. Bristowe, A. K. Cheetham, H. M. Jang, *Chem. Mater.* **2016**, 28, 4259.
- [52] E. J. Sie, C. M. Nyby, C. D. Pemmaraju, S. J. Park, X. Shen, J. Yang, M. C. Hoffmann, B. K. Ofori-Okai, R. Li, A. H. Reid, S. Weathersby, E. Mannebach, N. Finney, D. Rhodes, D. Chenet, A. Antony, L. Balicas, J. Hone, T. P. Devereaux, T. F. Heinz, X. Wang, A. M. Lindenberg, *Nature* **2019**, 565, 61.
- [53] J. Gong, M. Yang, D. Rebollar, J. Rucinski, Z. Liveris, K. Zhu, T. Xu, *Adv. Mater.* **2018**, 30, 1800973.
- [54] N. Holtgrewe, E. Greenberg, C. Prescher, V. B. Prakapenka, A. F. Goncharov, *High Pressure Res.* **2019**, 39, 457.
- [55] G. Kresse, J. Furthmüller, *Phys. Rev. B* **1996**, 54, 11169.
- [56] G. Kresse, J. Furthmüller, *Comput. Mater. Sci.* **1996**, 6, 15.
- [57] G. Kresse, J. Hafner, *Phys. Rev. B* **1994**, 49, 14251.
- [58] G. Kresse, J. Hafner, *Phys. Rev. B* **1993**, 47, 558(R).
- [59] J. P. Perdew, K. Burke, Y. Wang, *Phys. Rev. B* **1996**, 54, 16533.
- [60] P. Hohenberg, W. Kohn, *Phys. Rev.* **1964**, 136, B864.
- [61] P. E. Blöchl, *Phys. Rev. B* **1994**, 50, 17953.
- [62] J. Klimeš, D. R. Bowler, A. Michaelides, *Phys. Rev. B* **2011**, 83, 195131.
- [63] A. Togo, I. Tanaka, *Scr. Mater.* **2015**, 108, 1.
- [64] N. Onoda-Yamamuro, T. Matsuo, H. Suga, *J. Phys. Chem. Solids* **1990**, 51, 1383.